RESEARCH ARTICLE



Phase transition of $SrCo_{0.9}Fe_{0.1}O_3$ electrocatalysts and their effects on oxygen evolution reaction

Cheng Zhang¹ | Fangfang Wang^{1,2} | Mariam Batool¹ | Beichen Xiong¹ | Hong Yang¹

²School of Mechanical and Power Engineering, Zhengzhou University, Zhengzhou, Henan Province, P. R. China

Correspondence

Hong Yang, Department of Chemical and Biomolecular Engineering, University of Illinois at Urbana-Champaign, 600 S. Mathews Avenue, Urbana, IL 61801, USA. Email: hy66@illinois.edu

Funding information

US National Science Foundation, Grant/Award Number: NSF-2055734; University of Illinois at Urbana-Champaign; China Scholarship Council (CSC); Higher Education Commission of Pakistan (HEC)

Abstract

Complex metal oxide has emerged as an important class of electrocatalyst for oxygen evolution reaction (OER) because of its flexibility in the crystal phase and relative ease in the control of defect structures. While different crystalline phases and solid structures may be produced from the same reactant precursors, their phase transitions and OER performances are not well understood. In this work, we present the preparation of different phases of $SrCo_{0.9}Fe_{0.1}O_{3-\delta}$ (nominal ratio) solids using a sol-gel method and the structure-catalytic property relationship of both crystalline and amorphous structures formed at different temperatures. We observed as synthetic temperature increased, phase and composition transitions occurred from the amorphous phase to strontium carbonate and cobalt oxide, to oxygen-deficient perovskite, and finally to perovskite. The OER activity depended highly on crystal structures. The oxygen-deficient perovskite prepared at 750°C exhibited the highest catalytic activity, while the perovskite showed the lowest activity. X-ray photoelectron spectroscopy analysis reveals the change of oxidation state occurred during the phase transition. This work provides a useful guideline for the design of OER electrocatalysts through controlling the crystal structures and defects in complex metal oxides, such as perovskite.

KEYWORDS

metal substitution, oxygen evolution reaction, oxygen vacancy, perovskite, phase transition

1 | INTRODUCTION

Development of high-performance electrocatalysts of oxygen evolution reaction (OER) is essential for various sustainability applications, including water electrolyzer for low-temperature green hydrogen generation. The sluggish kinetics of OER together with the requirement in durability under harsh operating conditions hinder the

widespread applications of water electrolysis at the industrial scale. Currently, IrO₂ and, to a lesser extent, RuO₂ are used as OER catalysts in industries and they are also served as the benchmark catalysts. Scarcity of these noble metals further limits their potential use at large scale. Thus, the production of OER catalysts with high performance but free of noble metals remains the major challenge. Great effort has been devoted to the develop-

This is an open access article under the terms of the Creative Commons Attribution License, which permits use, distribution and reproduction in any medium, provided the original work is properly cited.

© 2022 The Authors. SusMat published by Sichuan University and John Wiley & Sons Australia, Ltd.

¹Department of Chemical and Biomolecular Engineering, University of Illinois at Urbana-Champaign, Urbana, Illinois, USA

ment of new electrocatalysts and the reaction mechanisms in recent years, aiming to improve the OER kinetics.

Non-noble metal-based perovskite could potentially be a promising class of materials for electrocatalysis because of its high tolerance of structural defects, and tunable conductive properties.^{20–30} The flexibility in crystal and electronic structures are in fact important considerations, when perovskite is used for catalysis applications. Generally, perovskite (ABO₃) exhibits either cubic or orthorhombic structure. By conducting redox chemistry, defects could be introduced in perovskite at low temperature to produce oxygen-deficient solid, which exhibited the enhanced OER activity.³¹ In addition, metal doping can help change the electronic or even crystalline structures, thus the OER kinetics, of complex metal oxides, which include perovskite, pyrochlore, and Ruddlesden-Popper phase oxides, to name a few. ^{22,24,29,32–36} Origins for the enhancement in OER performance from these complex metal oxides are often complicated and involved oxygen species, and multiple new theories have been developed in recent years.^{37–43} A lattice oxygen-mediated mechanism (LOM) has become a commonly accepted one, which suggests lattice oxygen is involved in the OER process. Compared with the adsorbate evolution mechanism (AEM), which suggests only metal center participates in the reaction, LOM provides an alternative angle in the design of OER electrocatalysts, in which a lowered energy barrier is feasible and the OER kinetics could be faster than those predicted by the AEM. Oxygen vacancy was considered to be directly relevant to the LOM in the observed high catalytic activity. Besides, doping of transition metal elements in complex metal oxides, such as perovskite, could change the electronic structures to favor the electron transfer in the OER. 27,44-46 In addition, the change of the structural property often favors the formation of (oxy)hydroxide layer on the surface, which is a key feature for the high OER activity in the alkaline system. 47-50 Although different crystal structures of complex metal oxides, including lattice defects, can be obtained by controlling the synthetic conditions, the effect of the phase transition of perovskite on OER performance was not well studied.

Herein, we investigate the effects of temperature on the preparation of various solid structures and their corresponding OER activities of $SrCo_{0.9}Fe_{0.1}O_3$ perovskite. The $SrCo_{0.9}Fe_{0.1}O_3$ electrocatalysts were synthesized starting with the sol–gel method, followed by reactions at a predetermined temperature of 250, 500, 750, and $1050^{\circ}C$, respectively. The obtained solids were denoted as SCFO-x, where x is the synthetic temperature. The analysis on the crystal structures revealed this series of solids underwent a phase transition as temperature increased, from amorphous solid, to a mixture of strontium carbonate and cobalt oxide, to an oxygen-deficient perovskite, and finally

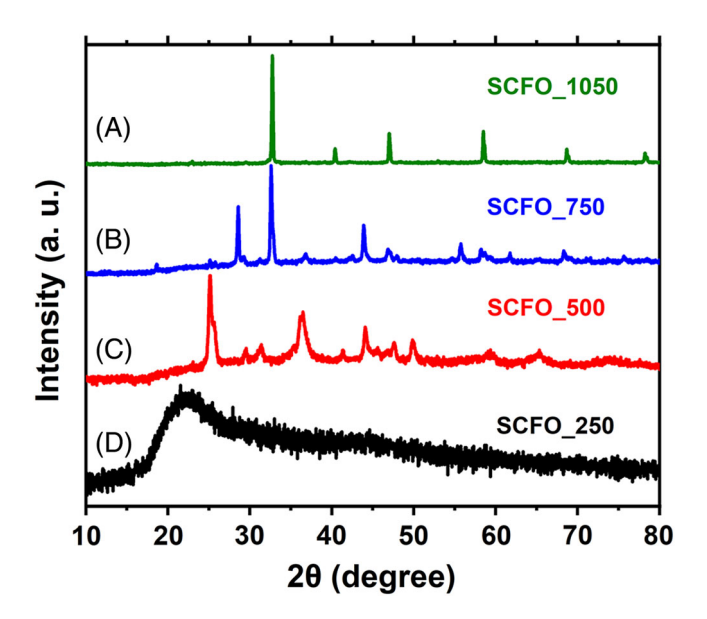


FIGURE 1 XRD patterns of (A) amorphous phase SCFO-250, (B) SCFO-500 containing the mixed orthorhombic SrCO₃ and cubic Co₃O₄, (C) SCFO-750 of oxygen deficient perovskite, and (D) SCFO-1050 of cubic perovskite, respectively

to perovskite. Electrochemical measurements indicate that SCFO-*x* prepared at different temperatures showed distinct OER activities and the oxygen deficiencies in perovskite could result in high OER activities. In addition, amorphous catalyst prepared at low temperature exhibited high OER kinetics, resulting from the large amount of active sites. X-ray photoelectron spectroscopy (XPS) data indicate the electronic configuration and lattice structures changed as temperature increased, which could lead to the observed OER activity.

2 | RESULTS AND DISCUSSION

The sol-gel method was applied to synthesize this series of OER electrocatalysts. Metal precursors with predetermined stoichiometric ratios were mixed in water with citric acid. Ammonium hydroxide was added to adjust the pH of the reaction solution to be between 8 and 10. Water in these reaction mixtures was allowed to evaporate to form the gel at 80°C. The SCFO-250 solid was prepared after heating the obtained gel at 250°C for 5 h, while SCFO-500, SCFO-750, and SCFO-1050 were prepared by calcinating SCFO-250 at 500, 750, and 1050°C, respectively, for a reaction time of 12 h. Figure 1 shows the powder X-ray diffraction (XRD) patterns of these SCFOx solids. There was no obvious diffraction peak identified for SCFO-250, except a broad peak around 22° 2θ, which could be assigned to carbon-containing species. This result indicates that SCFO-250 is made of an amorphous

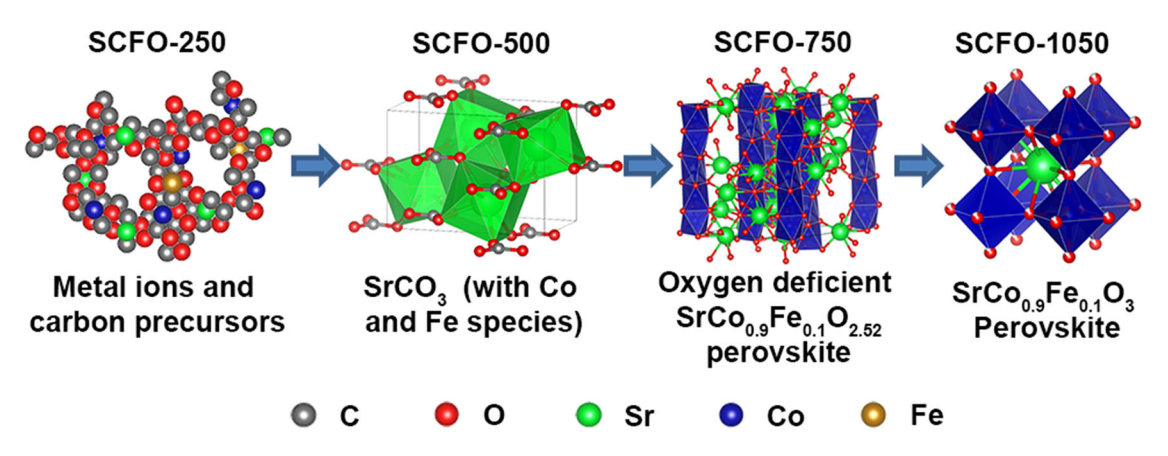


FIGURE 2 Illustration of structure and phase transition of SCFO-x as a function of synthetic temperature, from amorphous phase to oxygen-deficient perovskite, and to cubic perovskite

mixture from citric acid and the metal element precursors. The XRD of SCFO-500 shows distinct patterns that can be assigned mainly to orthorhombic phase strontium carbonate (SrCO₃, PDF#: 01-084-1778). The broad diffraction peaks located around 59° and 65° 2θ could come from the low-crystalline phase of the cubic phase cobalt oxide (Co₃O₄, PDF#: 01-078-1969) (Figure S1). Iron species was not detected by the XRD pattern, likely due to the low amount of the Fe precursor used in the reaction mixture. The XRD pattern of SCFO-750 matches well with the hexagonal-phase oxygen-deficient perovskite (SrCoO_{2.52}, PDF#: 00-040-1018), indicating the oxygen vacancies, and the δ value in $SrCo_{0.9}Fe_{0.1}O_{3-\delta}$ should be close to 0.48 for SCFO-750 (Figure S2). In comparison, the XRD characterization indicates that the SCFO-1050 catalyst is cubic perovskite (PDF#: 00-046-0335; Figure S3). The energydispersive X-ray fluorescence (EDXRF) data indicate that the atomic ratio of metal elements in the product agreed with the feeding ratios (Table S1).

The structural change of the crystal phase of these SCFO-x solids as a function of reaction temperature is illustrated in Figure 2. The aerogel formed at 80°C upon the initial hydrolysis and condensation. After the heat treatment at 250°C for 5 h to form oxides or hydroxides via the decomposition of metal precursors and critic acid, the SCFO-250 in the amorphous structure was obtained. With further heat treatment at 500°C, a mixture made of SrCO₃ and Co₃O₄ crystal structures formed. Iron species could exist as doped species, which were undetectable by XRD. Oxygen-deficient perovskite was prepared when reaction took place at 750°C. The SCFO-750 solid shows a hexagonal structure, which was identified as an intermediate structure between cubic perovskite and orthorhombic Brownmillerite (PDF#: 00-040-1018),³² containing oxygen vacancies in the crystal structure (Figure 2). The cubic perovskite structure of SCFO-1050 formed at 1050°C. In comparison with the synthesis of SrCo_xFe_{1-x}O₃ previously reported,²⁵ this perovskite structure appeared at a higher temperature, which suggests that the formation of perovskite depends on the ratio of metal precursors.

Figure 3 shows the characterizations of morphology and the elemental distributions of these catalysts using scanning electron microscopy (SEM), and energy-dispersive X-ray spectroscopy (EDS). The SEM image shows that SCFO-250 has the typical morphology of a dried sol-gel production (Figure 3A). Figure 3B shows that SCFO-500 electrocatalyst is made of solid pieces with average size smaller than 1 μ m. SEM images show that SCFO-750 and SCFO-1050 have the morphologies that are often observed for crystalline solids (Figure 3C,D). The average particle size of SCFO-750 is around 200 nm, while the typical size for SCFO-1050 solid particles is 2–5 μ m. The SEM-EDS study was conducted to determine the elemental composition of these SCFO-x catalysts (Figure 3E-H). The elemental mapping demonstrates that all metal elements (Sr, Co, and Fe) and oxygen were uniformly distributed in the samples.

Transmission electron microscopy (TEM) was conducted to examine the crystal structure of SCFO-x electrocatalysts (Figures 4 and S4). The TEM study shows that the SCFO-250 sample contained largely amorphous materials with some low crystalline nanoparticles formed at low reaction temperatures (Figure S4a). The ring patterns in selected area electron diffraction (SAED) indicate the presence of the low-crystalline structure together with the amorphous solid (Figure S4c). The SCFO-500 sample was polycrystalline in nature, as being demonstrated by the lattice fringes (Figure S4c) and spotted SAED (Figure S4d). Figure 4A,B shows the TEM images of SCFO-750 and SCFO-1050 samples, respectively, both of which exhibit crystalline lattices. The *d*-spacing was measured to be 2.75 Å for the SCFO-750 sample (Figure 4A), which agrees well with the d-spacing of (110) plane of oxygen-deficient perovskite in the hexagonal phase (also see XRD, PDF#:

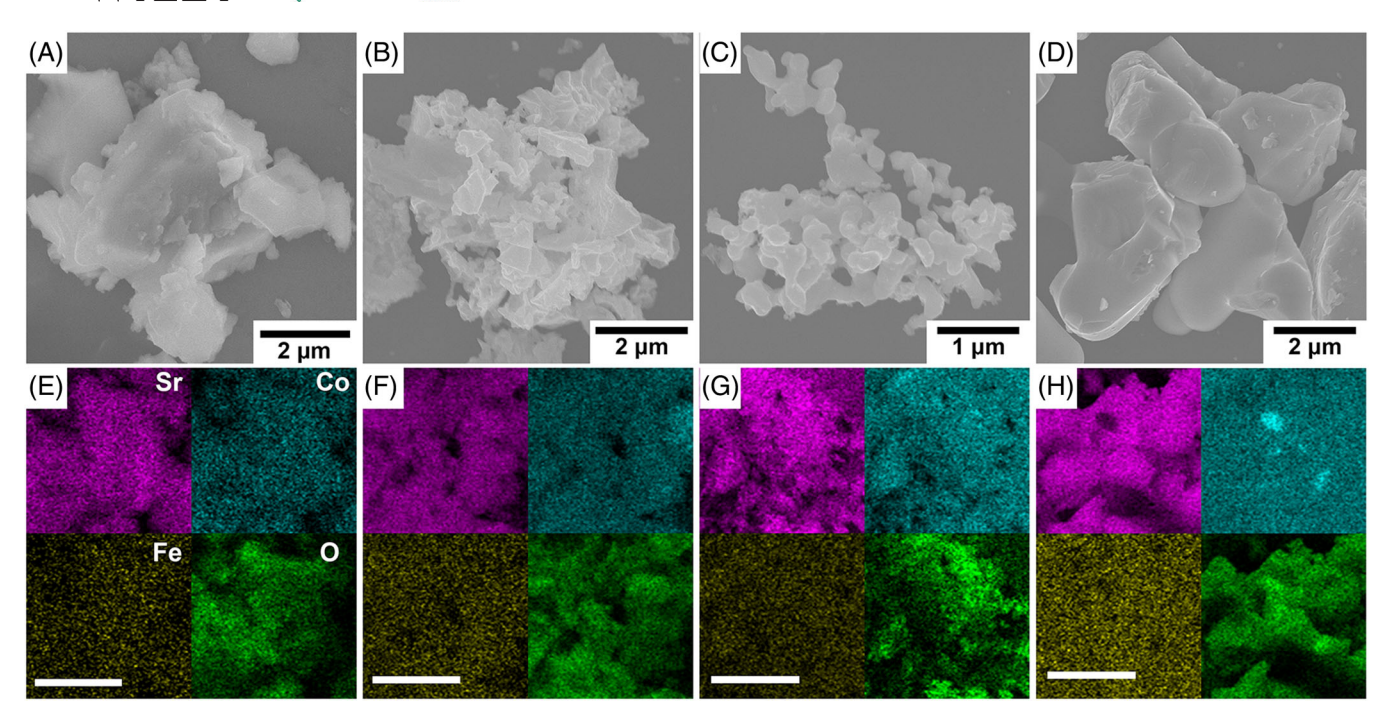


FIGURE 3 (A–D) Scanning electron microscopy (SEM) images and (E–H) SEM-EDS mapping of (A, E) SCFO-250, (B, F) SCFO-500, (C, G) SCFO-750, and (D, H) SCFO-1050. The scale bar in SEM-EDS mapping is $5 \mu m$

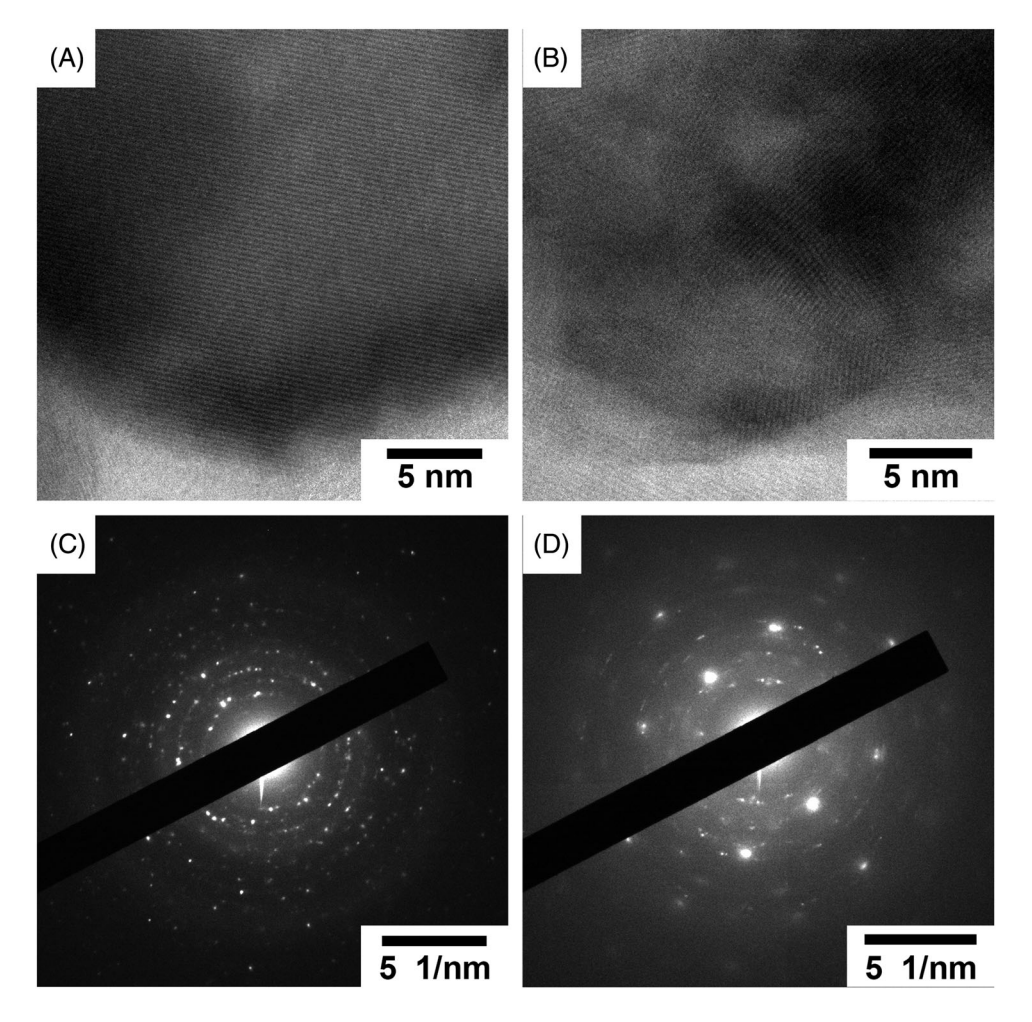


FIGURE 4 (A, B) Transmission electron microscopy (TEM) images and (C, D) SAED patterns of (A, C) SCFO-750, and (B, D) SCFO-1050

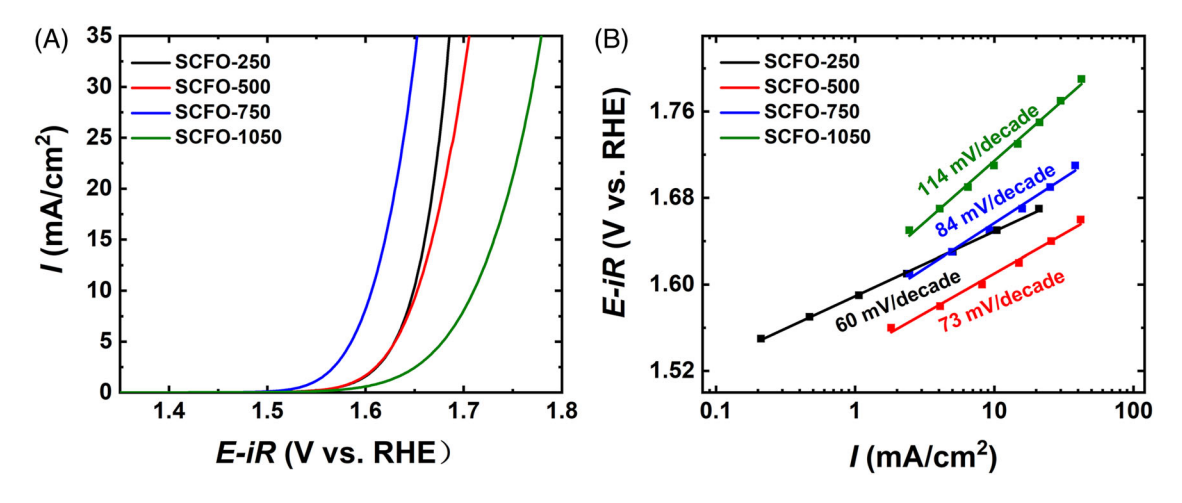


FIGURE 5 (A) Polarization curves and (B) Tafel slopes of the series of SCFO-*x* electrocatalysts with amorphous (SCFO-250), defect-rich (SCFO-750, perovskite), and crystalline (SCFO-500, SrCO₃/Co₃O₄ and SCFO-1000, perovskite) phases

00-040-1018). The SAED shows that this sample exhibits bright spotted pattern, indicating that the SCFO-750 material is polycrystalline (Figure 4C). The lattice spacing for the SCFO-1050 specimen was determined to be 2.78 Å, which also corresponds to the (110) plane of the perovskite structure (Figure 4B). The SAED pattern of SCFO-1050 exhibits only regular electronic diffraction spots, indicating that the catalyst is composed of much larger size grains with higher crystallinity than the samples made under other conditions.

The OER performance of SCFO-x catalysts was tested in 1 M KOH aqueous solution using a standard threeelectrode system. Figure 5A shows the polarization curves of these SCFO-x electrocatalysts. Among the series, the defective perovskite SCFO-750 electrocatalyst exhibits the highest OER activity and the lowest onset potential of 1.51 V. Interesting, the amorphous phase SCFO-250 exhibited the second lowest onset potential of around 1.55 V, closer (than the other two) to the SCFO-750 catalyst. At the current density of 10 mA/cm², the potential is 1.60 V for the oxygen-deficient perovskite (SCFC-750), 1.65 V for the amorphous phase sample (SCFO-250), and 1.66 V for SCFO-500. The perovskite SCFO-1050 was shown to be the least active catalyst, exhibiting an onsite potential of 1.58 V and a working potential of 1.71 V at the current density of 10 mA/cm². Figure 5B shows the Tafel slopes of these SCFO-*x* electrocatalysts. The amorphous phase SCFO-250 exhibited the smallest Tafel slope of 60 mV/dec, which could result in fast OER kinetics and large current density in the high-voltage range in the polarization curve (Figure 5A). The defective perovskite SCFO-750 electrocatalyst exhibited a Tafel slope of 84 mV/dec, while the strontium carbonate/cobalt oxide mixed solid (SCFO-500) had a value of 73 mV/dec. The perovskite SCFO-1050 had

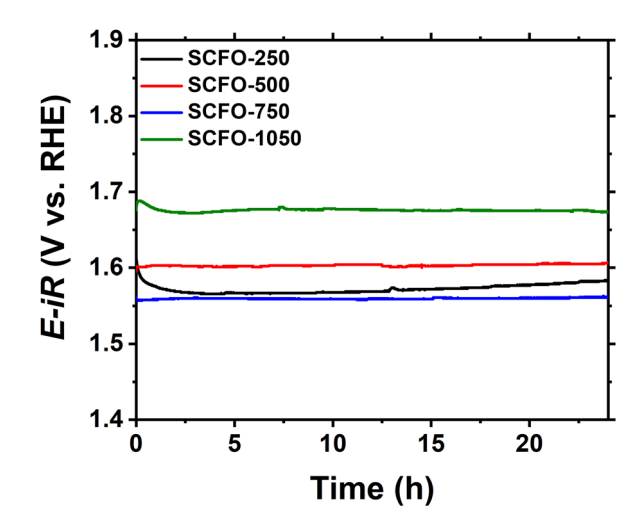


FIGURE 6 Chronopotentiometry performance of the SCFO-*x* electrocatalysts under constant current density of 10 mA/cm² for a period of 24 h, showing the oxygen-deficient perovskite had the lowest overpotential

the largest Tafel slope of 114 mV/dec, contributing to its poor OER activity.

Figure 6 shows the results of chronopotentiometry study of these SCFO-*x* electrocatalysts conducted at a constant current density of 10 mA/cm². All the catalysts retained the working potentials fairly well for the measurement period of 24 h, indicating a good stability in alkaline media. The working potential is 1.58 V for the SCFO-250, 1.60 V for the SCFO-500, 1.56 V for the SCFO-750, and 1.68 V for the SCFO-1050 electrocatalyst. This trend in OER overpotential agrees well with that determined using the polarization curves (Figure 5A). The slight increased overpotential of SCFO-*x* could be resulted from the Sr dissolution in the electrolyte solution, resulting in the formation of the

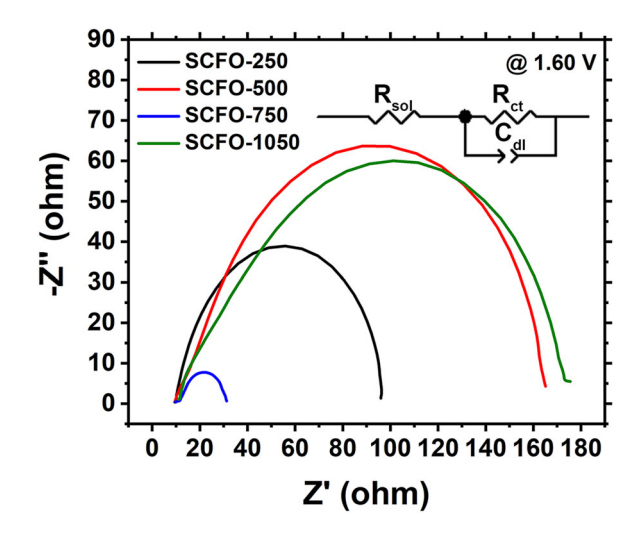


FIGURE 7 Nyquist plots measured at 1.60 V of the various SCFO-x electrocatalysts

amorphous layer on the surface. The amorphous phase consists of cobalt oxides formed after the dissolution of Sr in the crystal structures. Cobalt or Fe-based (oxy)hydroxide, which is a highly active species towards OER, could also form in the alkaline electrolyte solution on the surface of electrocatalysts.^{32,51}

Electrochemical impedance spectroscopy (EIS) measurements were conducted to gain a better understanding of the effects of impedance on the OER activity of these SCFO-*x* electrocatalysts. Figure 7 shows the Nyquist plots of the samples measured at 1.60 V, a potential slightly higher than that of the OER onsite potentials for all the SCFO-x catalysts. In the EIS measurement, charge transfer resistance (R_{ct}) reflects the kinetics of the charge transfer on the surface of the catalysts (Table S2). Among the series of samples, SCFO-750 shows the lowest R_{ct} value of 20.03 Ω , indicating the lowest electrochemical resistivity at this working potential. The large number of oxygen deficiencies and the high covalency of Co 3d and O 2p orbitals of SCFO-750 could be the key reasons attributing to the fast electron transfer on the surface of electrocatalysts.³² The SCFO-250 also shows a relatively low $R_{\rm ct}$ value of 89.02 Ω , while the $R_{\rm ct}$ is 160.6 Ω for SCFO-500 and 177 Ω for SCFO-1050. The relatively low R_{ct} of SCFO-250 could be resulted from the highly conductive amorphous structures and the small particle size (Figure S4a), which might facilitate the electron transfer. The EIS results suggest that the catalysts with high OER performance also possess low impedance at the operating potentials. It seems that the impedance plays an important role in affecting the OER kinetics.

Double layer capacitance ($C_{\rm dl}$) of the SCFO-x electrocatalysts were measured to gauge the electrochemically active surface area (ECSA) in order to gain understandings of the intrinsic surface activity. Figure 8 shows the cyclic

voltammogram (CV) scans of the four SCFO-x samples in a region without Faradic current. Different scan rates were tested and their corresponding linear fitting is summarized in Figure 8E. The SCFO-750 catalyst shows the highest $C_{\rm dl}$ of 1.25 mF/cm², likely resulting from its small average particle size, as shown in Figure 3C. The SCFO-250 sample exhibits a $C_{\rm dl}$ of 0.78 mF/cm², which could be attributed to the amorphous structures and the small crystalline domain. On the other hand, the $C_{\rm dl}$ value is small for both SCFO-500 and SCFO-1050 samples, and was determined to be 0.33 mF/cm² for SCFO-500 and 0.24 mF/cm² for SCFO-1050. The large particle size and reduced conductivity could be the main reasons. Figure 8F summarizes the OER activity normalized by the corresponding $C_{\rm dl}$ value. The results indicate that the oxygen-deficient perovskite SCFO-750 still exhibits the highest intrinsic surface activity at low potential. On the other hand, the activity trend for the other three samples changed. While SCFO-1050 still exhibited lowest intrinsic activity among the series, SCFO-500 shows higher intrinsic activity than SCFO-250. Because of the lower Tafel slope of SCFO-500 than SCFO-750, SCFO-500 even shows higher intrinsic activity than SCFO-750 at higher potentials.

The effects of main structural factors on the OER performance of these SCFO-x prepared at different temperatures could be analyzed based on the above characterizations and electrochemical measurements. Oxygen-deficient perovskite SCFO-750 exhibits the highest OER activity, as shown in the polarization curve in Figure 5A. The small particle size, low impedance at operating potentials, and the large $C_{\rm dl}$ likely attributed to the high activity. Besides, the oxygen vacancies of SCFO-750 facilitate the LOM kinetics during the reaction, often resulting in a lowered energy barrier than that determined solely by the conventional AEM.^{2,37} It was reported that this oxygendeficient structure is an intermediate between perovskite and brownmillerite and helps increase the covalency between Co 3d and O 2p orbitals, which is beneficial to the OER performance.³² Thus, oxygen deficiency in perovskite favors high intrinsic activity. It is intriguing that the SCFO-250 exhibits the lowest Tafel slope among these samples, which could result in a high OER activity at high working potential ranges. We hypothize that the fast OER kinetics could be attributed to the amorphous structure of this catalyst formed at a low temperature. The organic species in this mixture could provide a large number of sites for the formation of metal (oxy)hydroxide, one major active species for catalyzing the OER in alkaline media. This amorphous structure tends to possess high surface area as well because of a low degree of condensation reaction and therefore, a large $C_{\rm dl}$ value, which also facilitates fast OER kinetics. The formation of metal (oxy)hydroxides on the surface could also be the main reason for high

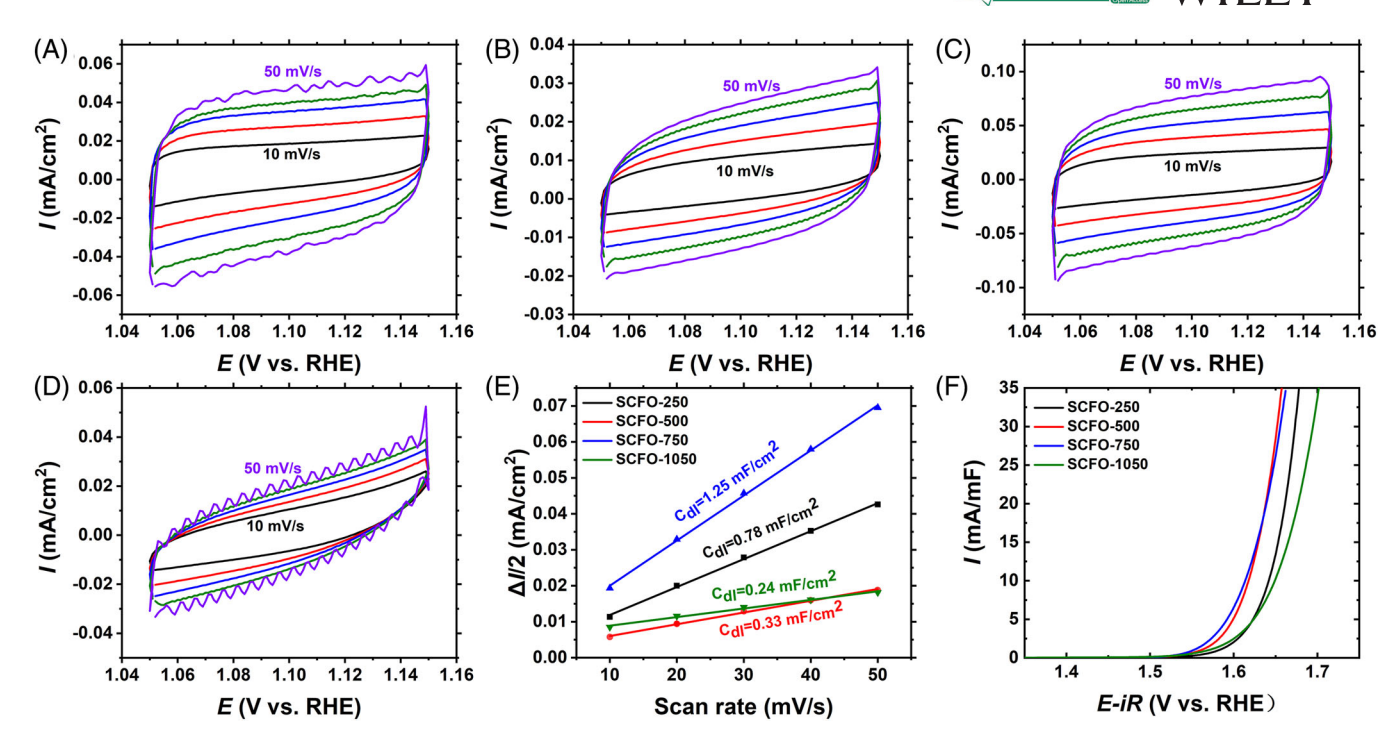


FIGURE 8 Cyclic voltammogram (CVs) measured in a non-Faradic current region (1.05–1.15 V vs. RHE) at a scan rate of 10, 20, 30, 40, and 50 mV/s, respectively, for (A) SCFO-250, (B) SCFO-500, (C) SCFO-750, and (D) SCFO-1050; (E) linear fitting curves of the capacitive current as a function of scan rate; and (F) intrinsic activity of these SCFO-*x* electrocatalysts normalized by $C_{\rm dl}$

intrinsic activity for the SCFO-500 sample. However, the large impedance of metal oxide and carbonate leads to a small number of active sites on the surface, resulting in the lowered specific activity. Perovskite SCFO-1050 shows the lowest activity in the series, resulted from the poor kinetics as confirmed by the large Tafel slope and high impedance and small ECSA.

XPS was conducted to examine the change of electronic structures of these catalysts that formed in the temperature-dependent phase transition process. Figure S5 shows the survey scans of these SCFO-*x* samples. The peak centered around 285 eV was from carbon. Its intensity was the strongest for SCFO-250, decreased for SCFO-500, and even further in SCFO-750 and SCFO-1050, indicating a high level of carbon species in SCFO-250 and SCFO-500. The high carbon population in SCFO-250 is related to the low peak intensity from the metal species, at around 135 eV for Sr, 715 eV for Fe, and 780 eV for Co.

Figure 9A and Table S3 show the XPS spectrum of Co 2p region, which was fitted into two peaks of Co $2p_{1/2}$ and Co $2p_{3/2}$, and one satellite peak of Co $2p_{3/2}$. The Co $2p_{3/2}$ satellite peak for the SCFO-250 sample was located at around 785 eV, which could be assigned to a low oxidation state close to Co(II). Since Co(II) salt was used as the precursor, this observation indicates that the valence of this metal ion remains unchanged in SCFO-250. This Co $2p_{3/2}$ satellite peak shifted to higher binding energy values of around 789 eV for the remaining three samples (SCFO-

500, 750, and 1050) as temperature increased, suggesting the oxidation state of cobalt ions increased after the reaction at high temperatures.⁵² Similarly, XPS spectroscopy of the Fe 2p region was also fitted into three peaks of Fe $2p_{1/2}$, Fe $2p_{3/2}$, and Fe $2p_{3/2}$ satellite. The location of Fe $2p_{3/2}$ satellite could be used to determine the oxidation state of iron ions (Figure 9b, Table S4). In general, Fe 2p_{3/2} satellite peak is located around 715 eV for Fe(II), and around 719 eV for Fe(III). The Fe $2p_{3/2}$ satellite peak was detected around 717.0 eV for the SCFO-250 sample because Fe(III) precursor was used in the synthesis. This peak shifted to a lower binding energy of 714.6 eV for SCFO-500, which might result from the reduction of iron ions during the calcination. This peak shifted to higher binding energy when the synthetic temperature increased to 1050°C, indicating the change in oxidation of iron species during this process. In addition, the position of Fe 2p_{3/2} satellite peak for SCFO-1050 became 716.5 eV, which could be from a mixture of Fe(II) and Fe(III) oxidation states.

Figure 9C and Table S5 show that the XPS spectrum of O 1s region was fitted into three peaks: oxide, hydroxyl group, and adsorbed water. The oxide peak could not be observed for SCFO-250, because this sample is made of mainly organics, metal oxide did not form at this low temperature. The XPS oxide peaks could be readily detectable for samples formed at high temperatures. As temperature increased, the oxide and adsorbed water peaks gradually diminished. SCFO-250 exhibits high ratio of hydroxyl

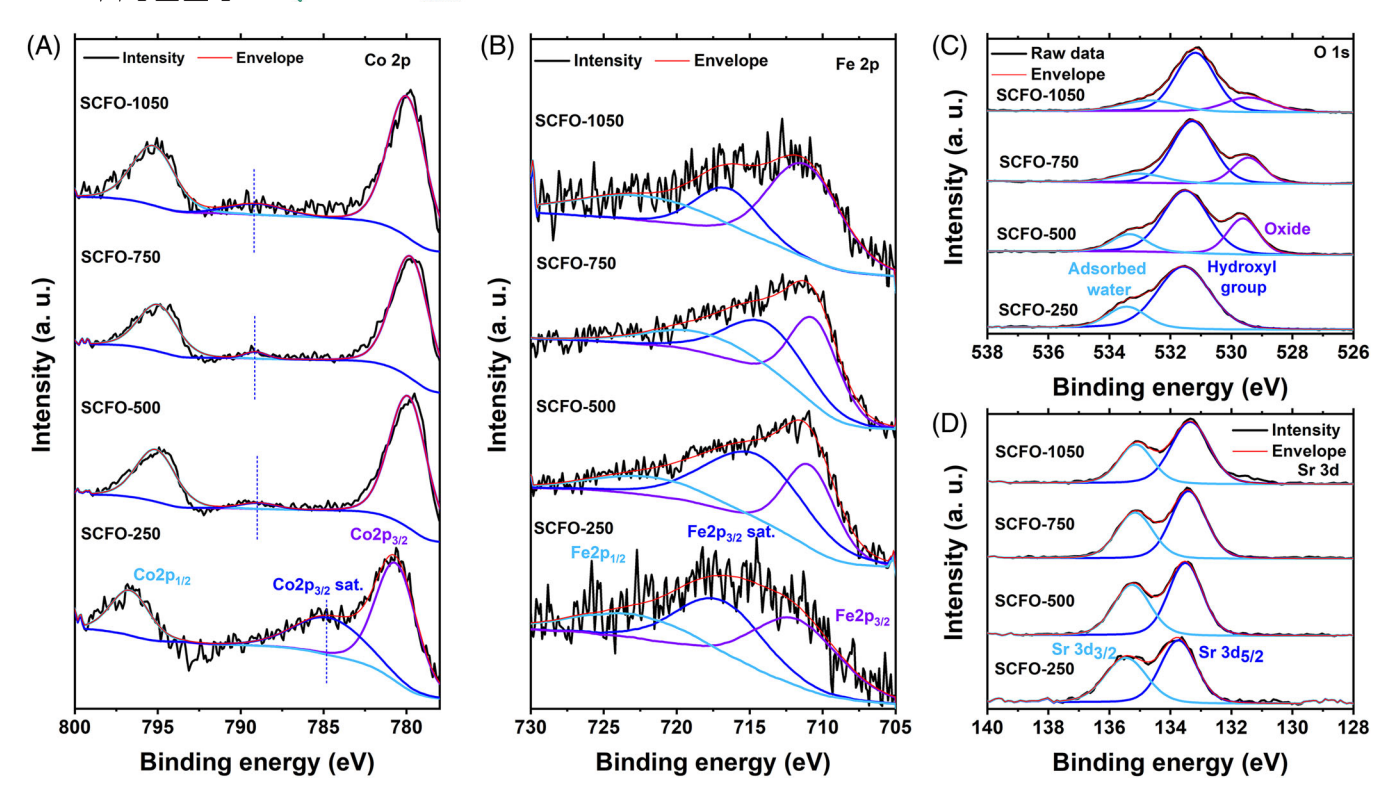


FIGURE 9 X-ray photoelectron spectroscopy (XPS) patterns of (A) Co 2p, (B) Fe 2p, (C) O 1s, and (D) Sr 3d regions of this series of SCFO-x samples

groups on the surface, which could contribute to the high intrinsic activity per active site as indicated by the low Tafel slope in Figure 5B. Since the SCFO-1050 catalyst exhibited the lowest OER activity, this result suggests that the surface hydroxyl groups should not be the determining factor on the catalytic performance. Figure 9D and Table S6 show the XPS signals from the Sr 3d region, which consist of Sr $3d_{3/2}$ and Sr $3d_{5/2}$ peaks. These peaks gradually shifted to low binding energy as temperature increased, indicating that Sr may be reduced during the synthesis.

3 | CONCLUSIONS

In summary, we synthesized a series of SCFO-x electrocatalysts for OER and investigated the phase transition and structure–property relationship during the structural evolution from the amorphous phase, to a mixture of strontium carbonate and cobalt oxide, to defective perovskite, and eventual perovskite as temperature increased. Among the electrocatalysts with similar elemental composition, the oxygen-deficient perovskite (SCFO-750) exhibited the highest catalytic activity, associated with low impedance and high level of oxygen vacancies, which are beneficial to the OER kinetics. The crystal phase transition was analyzed using XPS to examine the change of electronic structures of these serious samples. This study

provides a simple strategy of regulating the catalytic performance of complex metal oxides for OER electrocatalysis based on the effect of synthetic temperature on the crystal structure. Enhancement of activity through controlling the oxygen-defect chemistry and amorphous phase appears to be especially intriguing in the design of OER electrocatalysts.

4 | MATERIALS AND METHODS

4.1 | Materials

Iron (III) nitrate nanohydrate (Fe(NO₃)₃, 98%), strontium (II) nitrate (Sr(NO₃)₂, 99.0%), potassium hydroxide (KOH, 99.99%), and Nafion® 117 solution (\sim 5%) were purchased from Sigma–Aldrich. Cobalt (II) nitrate hexahydrate (Co(NO₃)₂·6H₂O, 98.0%) was purchased from Alfa Aesar. Citric acid monohydrate (C₆H₈O₇·H₂O, 99%) and sodium hydroxide (NaOH, 99.4%) were obtained from Fisher Chemical. Ammonium hydroxide (NH₄OH, 28.0%–30.0% as NH₃) and tetrahydrofuran (THF) were obtained from Macron Fine Chemicals. Vulcan carbon XC-72 was supplied from Cabot Corporation. Hydrogen (H₂, 99.999%) and oxygen (O₂, 99.999%) were purchased from Airgas, Inc. All the chemicals and gases were used without further purification.



4.2 | Synthesis

The SCFO-x solid powders were synthesized using a solgel method. In a typical experiment, 1 mmol (211.63 mg) of Sr(NO₃)₂ was mixed with 0.9 mmol (261.93 mg) of $Co(NO_3)_2 \cdot 6H_2O$ and 0.1 mmol (21.49 mg) of $Fe(NO_3)_3$ in 10 ml of water in a 50-ml beaker, followed by heating at 80°C under stirring for 30 min using an oil bath on top of a hotplate (VWR, Cat. No. 97042-714). The beaker was covered during this step. Citric acid (4 mmol, 768.48 mg) was then added to the solution and continued heating at this temperature for 30 min. After all precursors were dissolved and mixed well, ammonium hydroxide was added to adjust the pH value of the solution to 8-10. After this reaction step, the beaker was heated to 80°C using an oil bath on a hot plate for 5 h, followed by placing the beaker in a vacuum oven (VWR Symphony, E191047) at 120°C for 6 h to remove water. The dry solid was grinded with a pestle and mortar. The obtained fine powders were transferred into an alumina boat (Sigma-Aldrich, 5 ml) and heated in a tube furnace (Thermo Fisher Scientific™, Lindberg/Blue M™ Mini-Mite™) at 250°C for 5 h with a ramping rate of 5°C/min to obtain the SCFO-250 sample. After being grinded further for 5 min, the SCFO-250 sample was heated to 500, 750, and 1050°C to obtain the SCFO-500, SCFO-750, and SCFO-1050 solids, respectively. The ramping rate was 5°C/min and the heating time was 12 h in the tube furnace for this last step.

4.3 | Characterizations

Powder XRD analyses were conducted using a Rigaku Miniflex 600 diffractometer with Cu K α X-ray source (λ = 1.54056 Å). The scan range was between 10° and 80° 2θ and the scan rate was 0.04° 2 θ per second. High-resolution transmission electron microscopy (HR-TEM) studies were performed on a JEOL 2100 Cryo TEM with a LaB₆ emitter. The acceleration voltage for TEM measurements was 200 kV. A uniform dispersion of catalysts in ethanol was prepared by sonication, and one drop of this dispersion was deposited on carbon-coated TEM grids to prepare the TEM specimens. SEM images were obtained using a Hitachi S4800 microscope. The acceleration voltage of SEM was 10 kV. The powder samples were placed on the sample holder using conductive carbon tape. EDXRF results were collected using a Shimadzu EDX-700 spectrometer with Rh X-ray source by directly loading the powder samples in a polypropylene sample cup using a transparent ultralene film at the bottom of the sample cup. X-ray photoelectron spectroscopy (XPS) analysis was conducted on a Kratos Axis ULTRA system with an Al K α X-ray source. CasaXPS software was used for the data processing of the XPS results.

4.4 | Electrochemical measurements

All the electrochemical measurements were conducted in a three-electrode system using a CHI 760E potentiostat (CH Instruments, Inc.) with a platinum wire as the counter electrode and a reversible hydrogen electrode (RHE, Hydroflex) as the reference electrode. Working electrode is a rotating disk electrode (RDE) with catalysts loaded on the glassy carbon disc (0.196 cm²). One molar aqueous solution of KOH was used as the electrolyte. The RHE was calibrated in the electrolyte solution saturated with H_2 gas. The electrolyte was purged with O_2 for over 30 min to reach saturation before any of the electrochemical measurements. The ink was prepared by mixing 2 mg of catalysts, 2 mg of carbon black (XC-72), and 3 μ l of Nafion solution (pH = 7, neutralized using 0.1 M NaOH) in 2 ml of tetrahydrofuran (THF), followed by sonication in an ice bath for 30 min to uniformly disperse the ink. The working electrode with a thin film of the catalyst was prepared by depositing $5 \mu l$ of the obtained ink onto the working area of the RDE, followed by dropping $5 \mu l$ of Nafion THF solution (mixture of 3 μ l of neutralized Nafion solution and 2 ml of THF) twice onto the RDE.

The OER activity was evaluated by conducting CV measurements in the potential range between 1.1 and 1.8 V for 5 cycles at a scan rate of 10 mV/s with the RDE rotating speed of 1600 rmp. The third cycle of the CV scans was used for the evaluation of the OER activity to avoid the mass transfer limitation in the initial cycles. The average current of the anodic and cathodic scans was used to obtain the polarization curve to minimize the effect of the double-layer capacitance.

EIS measurements were performed at the potential of 1.60 V with a frequency range from 1×10^4 to 0.1 Hz. ZView software was used for the fitting of Nyquist plots. The equivalent electrical circuit is consisted of three components: solution resistance ($R_{\rm sol}$), charge transfer resistance ($R_{\rm ct}$), and double-layer capacitance ($C_{\rm cl}$).

The ECSA analysis was carried out by measuring double-layer capacitance ($C_{\rm dl}$) from the CV measurement. The CV scans were conducted at scan rates of 10, 20, 30, 40, and 50 mV/s, respectively, within a non-Faradic potential window between 1.05 and 1.15 V. The middle point between anodic and cathodic current densities was calculated at the potential of 1.10 V, and the obtained values were plotted against the scan rates. The slope of the linear fitting represented the $C_{\rm dl}$ values.

The stability of the OER catalysts was measured by performing chronopotentiometry tests at the current density of 10 mA/cm^2 using an electrode prepared with carbon paper. The electrode was made by depositing 750 μ l of ink onto a piece of carbon paper (Fuel Cell Store, Sigracet 22 BB) with a working area of 1×1 cm².

ACKNOWLEDGMENTS

This research was supported in part by the US National Science Foundation (NSF-2055734) and a start-up fund from University of Illinois at Urbana-Champaign. F.F. Wang was grateful for the support of a scholarship from the China Scholarship Council (CSC). M. Batool was funded by a fellowship from the Higher Education Commission of Pakistan (HEC). The X-ray diffraction was carried out at the George L. Clark X-ray Facility and 3M Material Laboratory, School of Chemical Science at UIUC. Other structural characterizations were performed at the Materials Research Laboratory at UIUC.

CONFLICT OF INTEREST

The authors declare no conflict of interest.

ORCID

Hong Yang https://orcid.org/0000-0003-3459-4516

REFERENCES

- 1. Song JJ, Wei C, Huang ZF, et al. A review on fundamentals for designing oxygen evolution electrocatalysts. *Chem Soc Rev.* 2020;49(7):2196-2214.
- Fabbri E, Schmidt TJ. Oxygen evolution reaction—The enigma in water electrolysis. ACS Catal. 2018;8(10):9765-9774.
- Krivina RA, Ou YQ, Xu QC, Twight LP, Stovall TN, Boettcher SW. Oxygen electrocatalysis on mixed-metal oxides/oxyhydroxides: From fundamentals to membrane electrolyzer technology. Acc Mater Res. 2021;2(7):548-558.
- 4. Suen NT, Hung SF, Quan Q, Zhang N, Xu YJ, Chen HM. Electrocatalysis for the oxygen evolution reaction: Recent development and future perspectives. *Chem Soc Rev.* 2017;46(2):337-365.
- 5. Blakemore JD, Crabtree RH, Brudvig GW. Molecular catalysts for water oxidation. *Chem Rev.* 2015;115(23):12974-13005.
- Matheu R, Garrido-Barros P, Gil-Sepulcre M, et al. The development of molecular water oxidation catalysts. *Nat Rev Chem*. 2019;3(5):331-341.
- Kondo M, Tatewaki H, Masaoka S. Design of molecular water oxidation catalysts with earth-abundant metal ions. *Chem Soc Rev.* 2021;50(12):6790-6831.
- 8. Li J, Guttinger R, More R, Song F, Wan W, Patzke GR. Frontiers of water oxidation: The quest for true catalysts. *Chem Soc Rev.* 2017;46(20):6124-6147.
- 9. Yu ZY, Duan Y, Feng XY, Yu XX, Gao MR, Yu SH. Clean and affordable hydrogen fuel from alkaline water splitting: Past, recent progress, and future prospects. *Adv Mater*. 2021;33(31):2007100.
- Kim J, Shih PC, Tsao KC, et al. High-performance pyrochloretype yttrium ruthenate electrocatalyst for oxygen evolution

- reaction in acidic media. *J Am Chem Soc.* 2017;139(34):12076-12083.
- 11. Kim J, Shih PC, Qin Y, Al-Bardan Z, Sun CJ, Yang H. A porous pyrochlore $Y_2[Ru_{1.6}Y_{0.4}]O_{7.\delta}$ electrocatalyst for enhanced performance towards the oxygen evolution reaction in acidic media. Angew Chem Int Ed. 2018;57(42):13877-13881.
- Sun YM, Liao HB, Wang JR, et al. Covalency competition dominates the water oxidation structure–activity relationship on spinel oxides. *Nat Catal*. 2020;3(7):554-563.
- Seitz LC, Dickens CF, Nishio K, et al. A highly active and stable IrO_x/SrIrO₃ catalyst for the oxygen evolution reaction. *Science*. 2016;353(6303):1011-1014.
- Shih PC, Zhang C, Raheja H, Sun CJ, Yang H. Polymer entrapment flash pyrolysis for the preparation of nanoscale iridium-free oxygen evolution electrocatalysts. *Chem Nano Mat*. 2020;6(6):930-936.
- Kim J, Chen XX, Pan YT, Shih PC, Yang H. W-doped CaMnO_{2.5} and CaMnO₃ electrocatalysts for enhanced performance in oxygen evolution and reduction reactions. *J Electrochem Soc.* 2017;164(12):F1074-F1080.
- 16. Oh HS, Nong HN, Reier T, et al. Electrochemical catalyst-support effects and their stabilizing role for IrO_x nanoparticle catalysts during the oxygen evolution reaction. *J Am Chem Soc.* 2016;138(38):12552-12563.
- 17. Lee Y, Suntivich J, May KJ, Perry EE, Shao-Horn Y. Synthesis and activities of rutile IrO₂ and RuO₂ nanoparticles for oxygen evolution in acid and alkaline solutions. *J Phys Chem Lett.* 2012;3(3):399-404.
- Ma Z, Zhang Y, Liu SZ, et al. Reaction mechanism for oxygen evolution on RuO₂, IrO₂, and RuO₂@IrO₂ core-shell nanocatalysts. *J Electroanal Chem.* 2018;819:296-305.
- Paoli EA, Masini F, Frydendal R, et al. Oxygen evolution on wellcharacterized mass-selected Ru and RuO₂ nanoparticles. *Chem Sci.* 2015;6(1):190-196.
- Hwang J, Rao RR, Giordano L, Katayama Y, Yu Y, Shao-Horn Y. Perovskites in catalysis and electrocatalysis. *Science*. 2017;358(6364):751-756.
- Bockris JO, Otagawa T. Mechanism of oxygen evolution on perovskites. J Phys Chem. 1983;87(15):2960-2971.
- Zhu KY, Wu T, Li MR, Lu RF, Zhu XF, Yang WS. Perovskites decorated with oxygen vacancies and Fe–Ni alloy nanoparticles as high-efficiency electrocatalysts for the oxygen evolution reaction. *J Mater Chem A*. 2017;5(37):19836-19845.
- 23. Wang Z, Hao Z, Shi F, Zhu K, Zhu X, Yang W. Boosting the oxygen evolution reaction through migrating active sites from the bulk to surface of perovskite oxides. *J Energy Chem.* 2022;69:434-441.
- Harn YW, Liang S, Liu SL, et al. Tailoring electrocatalytic activity of in situ crafted perovskite oxide nanocrystals via size and dopant control. *Proc Natl Acad Sci USA*. 2021;118(25):2014086118.
- Lin Q, Zhu YL, Hu ZW, et al. Boosting the oxygen evolution catalytic performance of perovskites via optimizing calcination temperature. J Mater Chem A. 2020;8(14):6480-6486.
- Badreldin A, Abusrafa AE, Abdel-Wahab A. Oxygen-deficient perovskites for oxygen evolution reaction in alkaline media: A review. *Emergent Mater*. 2020;3(5):567-590.
- Ede SR, Luo ZP. Tuning the intrinsic catalytic activities of oxygen-evolution catalysts by doping: A comprehensive review. *J Mater Chem A*. 2021;9(36):20131-20163.

- 28. Yang L, Yu GT, Ai X, et al. Efficient oxygen evolution electrocatalysis in acid by a perovskite with face-sharing IrO₆ octahedral dimers. *Nat Commun.* 2018;9:5236.
- 29. Edgington J, Schweitzer N, Alayoglu S, Seitz LC. Constant change: Exploring dynamic oxygen evolution reaction catalysis and material transformations in strontium zinc iridate perovskite in acid. *J Am Chem Soc.* 2021;143(26):9961-9971.
- 30. Kim J, Chen XX, Shih PC, Yang H. Porous perovskite-type lanthanum cobaltite as electrocatalysts toward oxygen evolution reaction. *ACS Sustain Chem Eng.* 2017;5(11):10910-10917.
- 31. Kim J, Yin X, Tsao KC, Fang SH, Yang H. Ca₂Mn₂O₅ as oxygen-deficient perovskite electrocatalyst for oxygen evolution reaction. *J Am. Chem. Soc.* 2014;136(42):14646-14649.
- 32. Ede SR, Collins CN, Posada CD, et al. Intermediate $Sr_2Co_{1.5}Fe_{0.5}O_{6-\delta}$ tetragonal structure between perovskite and brownmillerite as a model catalyst with layered oxygen deficiency for enhanced electrochemical water oxidation. *ACS Catal.* 2021;11(7):4327-4337.
- 33. She SX, Zhu YL, Wu XH, et al. Realizing high and stable electrocatalytic oxygen evolution for iron-based perovskites by Co-doping-induced structural and electronic modulation. *Adv. Funct. Mater.* 2021;32(15):2111091.
- 34. Ha MN, Lu GZ, Liu ZF, Wang LC, Zhao Z. 3DOM-LaSrCoFeO $_{6-\delta}$ as a highly active catalyst for the thermal and photothermal reduction of CO $_2$ with H $_2$ O to CH $_4$. *J Mater Chem A*. 2016;4(34):13155-13165.
- 35. Wang F, Zhang C, Yang H. Mixed B-site Ruddlesden-Popper phase $Sr_2(Ru_xIr_{1-x})O_4$ enables enhanced activity for oxygen evolution reaction. *J. Energy Chem.* 2022;70:623-629.
- 36. Zhang C, Wang F, Xiong B, Yang H. Regulating the electronic structures of mixed B-site pyrochlore to enhance the turnover frequency in water oxidation. *Nano Converg.* 2022;9:22.
- 37. Grimaud A, Diaz-Morales O, Han BH, et al. Activating lattice oxygen redox reactions in metal oxides to catalyse oxygen evolution. *Nat Chem.* 2017;9(5):457-465.
- Kuznetsov DA, Naeem MA, Kumar PV, Abdala PM, Fedorov A, Muller CR. Tailoring lattice oxygen binding in ruthenium pyrochlores to enhance oxygen evolution activity. J Am Chem Soc. 2020;142(17):7883-7888.
- Wen YZ, Chen PN, Wang L, et al. Stabilizing highly active Ru sites by suppressing lattice oxygen participation in acidic water oxidation. *J Am Chem Soc.* 2021;143(17):6482-6490.
- 40. Zhang N, Chai Y. Lattice oxygen redox chemistry in solidstate electrocatalysts for water oxidation. *Energy Environ Sci.* 2021;14(9):4647-4671.
- 41. Yoo JS, Rong X, Liu YS, Kolpak AM. Role of lattice oxygen participation in understanding trends in the oxygen evolution reaction on perovskites. *ACS Catal.* 2018;8(5):4628-4636.
- 42. Zhang P, Gong JL. Simple doping, great deal: Regulation of lattice oxygen for water splitting. *Chem.* 2018;4(12):2739-2741.

- 43. Shih PC, Kim J, Sun CJ, Yang H. Single-phase pyrochlore Y₂Ir₂O₇ electrocatalyst on the activity of oxygen evolution reaction. *ACS Appl Energy Mater.* 2018;1(8):3992-3998.
- 44. Zhang N, Wang C, Chen JW, et al. Metal substitution steering electron correlations in pyrochlore ruthenates for efficient acidic water oxidation. *ACS Nano*. 2021;15(5):8537-8548.
- Qu M, Ding XY, Shen ZC, et al. Tailoring the electronic structures of the La₂NiMnO₆ double perovskite as efficient bifunctional oxygen electrocatalysis. *Chem Mater*. 2021;33(6):2062-2071.
- 46. Ran J, Wang T, Zhang J, et al. Modulation of electronics of oxide perovskites by sulfur doping for electrocatalysis in rechargeable Zn–air batteries. *Chem Mater.* 2020;32(8):3439-3446.
- Kim BJ, Fabbri E, Abbott DF, et al. Functional role of Fe-doping in Co-based perovskite oxide catalysts for oxygen evolution reaction. *J Am Chem Soc.* 2019;141(13):5231-5240.
- 48. Lopes PP, Chung DY, Rui X, et al. Dynamically stable active sites from surface evolution of perovskite materials during the oxygen evolution reaction. *J Am Chem Soc.* 2021;143(7):2741-2750.
- 49. Kim BJ, Fabbri E, Borlaf M, et al. Oxygen evolution reaction activity and underlying mechanism of perovskite electrocatalysts at different pH. *Mater Adv.* 2021;2(1):345-355.
- Zhao JW, Li CF, Shi ZX, Guan JL, Li GR. Boosting lattice oxygen oxidation of perovskite to efficiently catalyze oxygen evolution reaction by FeOOH decoration. *Research*. 2020;2020: 6961578.
- Li HY, Chen YB, Ge JJ, et al. Active phase on SrCo_{1-x}Fe_xO_{3-δ} (0 ≤ x ≤ 5) perovskite for water oxidation: Reconstructed surface versus remaining bulk. *JACS Au*. 2021;1(1):108-115.
- Biesinger MC, Payne BP, Grosvenor AP, Lau LWM, Gerson AR, Smart RS. Resolving surface chemical states in XPS analysis of first row transition metals, oxides and hydroxides: Cr, Mn, Fe, Co and Ni. *Appl Surf Sci.* 2011;257(7):2717-2730.

SUPPORTING INFORMATION

Additional supporting information can be found online in the Supporting Information section at the end of this article.

How to cite this article: Zhang C, Wang F, Batool M, Xiong B, Yang H. Phase transition of SrCo_{0.9}Fe_{0.1}O₃ electrocatalysts and their effects on oxygen evolution reaction. *SusMat.* 2022;1–11. https://doi.org/10.1002/sus2.72